INTERNATIONAL JOURNAL OF REMOTE SENSING, 2016
VOL. 37, NO. 14, 3322–3345
http://dx.doi.org/10.1080/01431161.2016.1196842

Taylor & Francis
Taylor & Francis Group

Forest fuel treatment detection using multi-temporal airborne lidar data and high-resolution aerial imagery: a case study in the Sierra Nevada Mountains, California

Yanjun Su[a], Qinghua Guo[a], Brandon M. Collins[b,c], Danny L. Fry[d], Tianyu Hu[e] and Maggi Kelly[d]

[a]Sierra Nevada Research Institute, School of Engineering, University of California at Merced, Merced, CA, USA; [b]USDA Forest Service, Pacific Southwest Research Station, Davis, CA, USA; [c]Center for Fire Research and Outreach, University of California at Berkeley, Berkeley, CA, USA; [d]Department of Environmental Science, Policy, and Management, University of California at Berkeley, Berkeley, CA, USA; [e]State Key Laboratory of Vegetation and Environmental Change, Institute of Botany, Chinese Academy of Sciences, Beijing, China

ABSTRACT

Treatments to reduce forest fuels are often performed in forests to enhance forest health, regulate stand density, and reduce the risk of wildfires. Although commonly employed, there are concerns that these forest fuel treatments (FTs) may have negative impacts on certain wildlife species. Often FTs are planned across large landscapes, but the actual treatment extents can differ from the planned extents due to operational constraints and protection of resources (e.g. perennial streams, cultural resources, wildlife habitats). Identifying the actual extent of the treated areas is of primary importance to understand the environmental influence of FTs. Light detection and ranging (lidar) is a powerful remote-sensing tool that can provide accurate measurements of forest structures and has great potential for monitoring forest changes. This study used the canopy height model (CHM) and canopy cover (CC) products derived from multi-temporal airborne laser scanning (ALS) data to monitor forest changes following the implementation of landscape-scale FT projects. Our approach involved the combination of a pixel-wise thresholding method and an object-of-interest (OBI) segmentation method. We also investigated forest change using normalized difference vegetation index (NDVI) and standardized principal component analysis from multi-temporal high-resolution aerial imagery. The same FT detection routine was then applied to compare the capability of ALS data and aerial imagery for FT detection. Our results demonstrate that the FT detection using ALS-derived CC products produced both the highest total accuracy (93.5%) and kappa coefficient (κ) (0.70), and was more robust in identifying areas with light FTs. The accuracy using ALS-derived CHM products (the total accuracy was 91.6%, and the κ was 0.59) was significantly lower than that using ALS-derived CC, but was still higher than using aerial imagery. Moreover, we also developed and tested a method to recognize the intensity of FTs directly from pre- and post-treatment ALS point clouds.

ARTICLE HISTORY
Received 6 December 2015
Accepted 23 May 2016

CONTACT Qinghua Guo qguo@ucmerced.edu School of Engineering, University of California at Merced, 5200 North Lake Road, Merced, CA 95343, USA

© 2016 Informa UK Limited, trading as Taylor & Francis Group

1. Introduction

Forests of the Sierra Nevada mountain range in California, USA, are extensive, but face increasing risk of wildfire, largely due to fire suppression, fuel build-up, and changes in climate (Stephens, Millar, and Collins 2010). In 2013 alone, the American Fire and the Rim Fire burned over 111 km^2 of the Tahoe National Forest (located at the northern Sierra Nevada) and over 1,041 km^2 of forest in the Stanislaus National Forest and Yosemite National Park (located at the southern Sierra Nevada), respectively. To reduce the loss from uncharacteristically large and high-severity wildfire, the United States Department of Agriculture (USDA) Forest Service (referred to as USFS hereafter) and other land management agencies conduct mechanical forest fuel treatments (FTs) on areas with high fire risk in the Sierra Nevada. Through forest thinning and mastication, these mechanical FT activities aim to modify wild-land fire behaviours and minimize negative impacts on the forest health and enhance forest fire suppression capabilities (Collins et al. 2010). However, there have been concerns over potential negative impacts of these fire mitigation treatments on the habitat of protected animals, particularly the California spotted owl (*Strix occidentalis occidentalis*) and the Pacific fisher (*Martes pennant*).

Knowing the actual (as opposed to planned) extent of FTs (note that FTs referred to hereafter are mechanical FT activities) is critical for understanding how FTs affect the wildfire risk, wildlife, and forest health. The method for reporting completed FTs, which is still being used currently, involves using planned treatment boundaries and then updating them based on field observations. Planned FT boundaries are often geographically distinct from the actual extents due to operational constraints and the protection of resources (e.g. perennial streams, cultural resources, wildlife habitat). Thus, mapping the actual FT extent relies heavily on field observations, which are extremely labour-intensive and time-consuming processes. Moreover, currently, the intensity of FTs is commonly reported by FT types (e.g. low, crown, or selection thinning) (Agee and Skinner 2005) or harvesting methods (e.g. mastication, thinning, or cable thinning). Fundamentally, there remains a lack of accurate methods to quantitatively evaluate both the extent and the intensity of FTs.

Remote sensing, which can expand both spatial and temporal scales of land-surface observations, provides an alternative way to detect forest structure changes due to FTs. Change detection, defined as the process of identifying differences in the state of an object or a phenomenon by observing it at different times (Singh 1989), is the most commonly used method to identify land-surface changes from multi-temporal passive remote-sensing data. Generally, change detection can be divided into three groups: image algebra, transformation, and classification methods (Lu et al. 2004; Singh 1989). Image algebra methods apply algebraic calculus (e.g. image differencing, regression, ratioing) on multi-temporal remotely sensed data at the pixel level to obtain a change image (Allen and Kupfer 2000; Lunetta et al. 2006; Patra, Ghosh, and Ghosh 2011; Prakash and Gupta 1998; Sohl 1999). Transformation methods use statistical procedures [e.g. principal component analysis (PCA), Kauth–Thomas (KT) transformation, Gramm–Schmidt (GS) transformation, and chi-square transformation] to minimize the redundant information in multi-temporal data and derive change images (Collins and Woodcock 1994, 1996; Li and Yeh 1998; Qin et al. 2013; Ridd and Liu 1998; Seto et al. 2002). Both

algebra and transformation methods have to determine thresholds to differentiate the changed and unchanged areas (Guerra, Puig, and Chaume 1998; Yousif and Ban 2013). Classification methods identify change areas by comparing the image classification results from multi-temporal remote-sensing data (Desclée, Bogaert, and Defourny 2006; Hame, Heiler, and San Miguel-Ayanz 1998; Hao et al. 2014; Li and Xu 2010; Walter 2004). However, few studies have mapped FT areas using passive remote-sensing data because of the limited ability of these sensors for penetrating the forest canopy (Weishampel et al. 2000). Because FTs typically remove smaller and subdominant trees to reduce fuel laddering and use mastication of shrubs to remove surface fuels, the changes in forest surface spectral characteristics may be too slight to be identified with passive remote sensing.

Light detection and ranging (lidar), an active remote-sensing technique, uses a focused short wavelength laser pulse, which can penetrate the forest canopy more effectively. It has been proved that lidar can be used to accurately estimate forest parameters, such as tree height (Clark, Clark, and Roberts 2004; Hudak et al. 2002; Zimble et al. 2003), leaf area index (LAI) (Morsdorf et al. 2006; Riano et al. 2004; Richardson, Moskal, and Kim 2009; Zhao and Popescu 2009), and aboveground biomass (Bortolot and Wynne 2005; Popescu et al. 2011; Zhao, Popescu, and Nelson 2009). Clark, Clark, and Roberts (2004) used the airborne laser scanning (ALS) data to accurately estimate sub-canopy elevation and tree height in a tropical rainforest landscape. Korhonen et al. (2011) found that ALS discrete data can be used to obtain comparable estimations of forest vertical canopy cover (CC), angular canopy closure, and LAI. Andersen et al. (2005) estimated the canopy fuel parameters (e.g. crown fuel weight, crown bulk density, canopy height, and canopy base height) using regression analysis between ALS data-derived metrics and field measurements. Kramer et al. (2014) found that the forest percentage cover between 2 and 4 m derived from ALS data is a good indicator of ladder fuels, which are an important forest structural attribute contributing to wildfire hazard. Kane et al. (2013, 2014) evaluated the effects of wildfire on forest spatial structure at different height strata through the fusion of optical imagery and ALS data, and found that three forest spatial structures (i.e. canopy gap, clump-open, and open) were associated with the fire severity.

Accurate estimations of these forest parameters from ALS data are highly desirable for understanding the composition and structure information of forests and therefore monitoring forest changes (Dubayah et al. 2010). For example, Yu et al. (2004, 2006) estimated tree growths and monitored harvested trees using canopy height models (CHMs) derived from multi-temporal ALS data in a conifer forest. However, to the best of our knowledge, few studies have been conducted on using multi-temporal ALS to detect FT extents. Moreover, research comparing the capability of ALS data and aerial images for detecting FT extents is still lacking.

The main objective of this article is to study the capability of ALS data for identifying FTs using change detection routines that combine the pixel-wise thresholding (i.e. algebra or transformation methods) and the object-of-interest (OBI) segmentation (i.e. classification methods). As a comparison, the same change detection routine is also applied on multi-temporal high-resolution aerial imagery. Additionally, this study aims to investigate the possibility of quantitatively mapping the FT intensity directly from multi-temporal ALS data.

2. Data

2.1. *Study area*

The Last Chance study site (39°07′N, 120°35′W) covers 92.1 km^2 of the Tahoe National Forest, California, USA (Figure 1). It is on the southwest side of the Sierra Nevada crest. The elevation ranges from 228 m to 2189 m, and the slope ranges from 0° to close to 90°. Over 90% of the study area is covered by vegetation, and the average CC is around 67%. The study site is covered by mixed conifer forests, which are dominated by white fir (*Abies concolor*), ponderosa pine (*Pinus ponderosa*), incense cedar (*Calocedrus decurrens*), sugar pine (*Pinus lambertiana*), and Douglas fir (*Pseudotsuga menziesii*) (Su et al. 2016). Within the mixed conifer stands, the major hardwoods are black oak (*Quercus kelloggii*) and canyon live oak (*Quercus chrysolepis*) (Su et al. 2016). The FTs detected in the study area were implemented between 2008 and 2012. The main FTs conducted in this area were mechanical forest thinning, which aimed at reducing the ladder fuels by removing small to mid-sized trees from low and intermediate canopy strata within the treatment areas. It is important to note that these treatments intended to leave larger overstorey trees intact and have post-treatment CC between 40% and 50% (Collins et al. 2011).

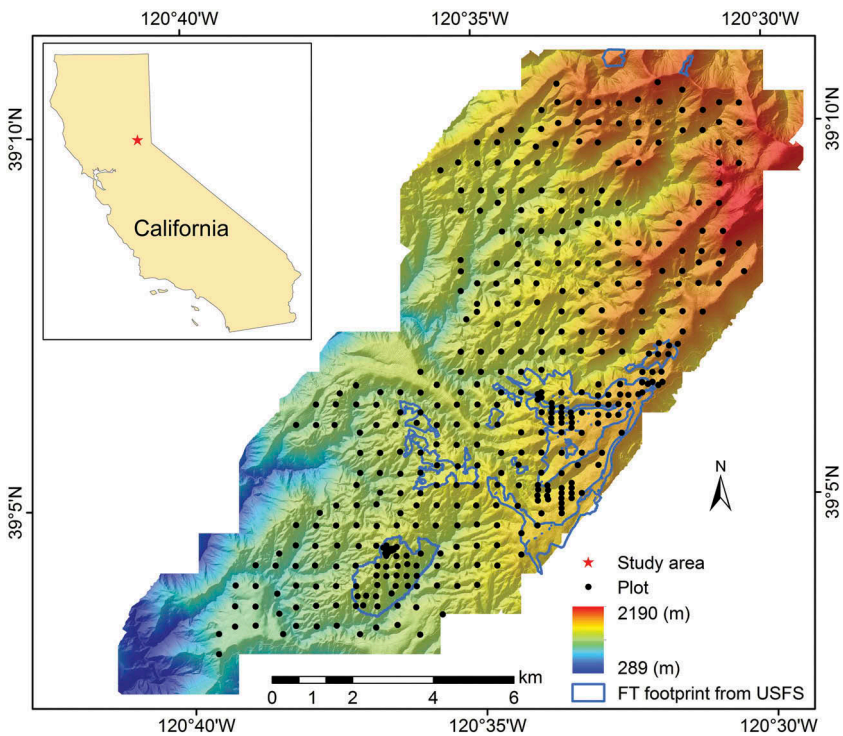

Figure 1. The Last Chance study area showing the distribution of field plots, terrain elevations, and the proposed forest fuel treatment (FT) footprints from the United States Forest Services (USFS).

2.2. *Field measurements*

A total of 408 plots (12.62 m in radius and 500 m^2 in area) were selected in the study site (Figure 1). The first plot was randomly chosen and the following plots were placed on 500 m × 500 m grids. Within specific watersheds, the sampling was intensified to 250 m × 250 m. When locating each plot by using a Trimble™ GeoXH GPS in the field, the plot centre had to be farther than 12.62 m away from any landing or road surfaces. If the plot needed to be offset, we randomly chose one of the four cardinal directions and moved the plot 25 m in that direction. In each plot, the CC measurement and the treatment condition were collected from the field. The CC was measured by a sight tube on a 5 m × 5 m regular grid centred on the plot centre (total of 25 points per plot). These measurements were made twice, first in the summer of 2007 (prior to treatment implementation) and again in 2013 (after treatment implementation). It should be noted that 39 plots were eliminated from the analysis of this study because their treatment conditions were not collected in the field. Among the remaining 369 plots, 46 plots were recognized as treated. Besides these plot measurements, polygons of the intended treatment areas (created by the USFS) were also used in this study to evaluate the FT detection accuracy (Figure 1).

2.3. *Small footprint ALS data*

The pretreatment ALS data used in this study were acquired in September 2007, and the post-treatment ALS data were acquired in November 2012 and August 2013 (the 2012 flight was stopped by snow). An Optech GEMINI airborne laser terrain mapper (ALTM) from National Center of Airborne Laser Mapping at the University of Houston was used for both pre- and post-treatment ALS data acquisition. The sensor was operated at 100 kHz with a scanning frequency of 40–60 Hz and a scan angle of 12–14° on either side of nadir. It was mounted on a twin-engine Cessna Skymaster, which flew at 600–800 m above the ground. The average swath width of a single pass was around 510 m with over 50% overlap between two adjacent flight lines, and the obtained point density was 9.6 points/m^2 on average. The ALS footprint size is about 15–20 cm in diameter. To ensure the pre- and post-treatment ALS flights aligned together, more than 800 ground checkpoints, positioned by ground GPS, were set to calibrate and assess the vertical and horizontal accuracies of the ALS flights. The obtained horizontal accuracy was around 10 cm and the vertical accuracy was from 5 to 35 cm.

Pre- and post-treatment CHM and CC products were calculated from ALS point clouds to detect FTs. To derive the CHM products, digital surface model (DSM) and digital elevation model (DEM) products were interpolated from the first returns and ground returns, respectively. The ground returns were identified using the software Terrascan following the standard industrial procedure. The interpolation scheme used was the ordinary Kriging algorithm, because it has been proved to be more accurate than other interpolation methods (such as inverse distance weighted and spline) for interpolating DEM and DSM from ALS-derived elevation points (Clark, Clark, and Roberts 2004; Lloyd and Atkinson 2002; Guo et al. 2010). The CHM was calculated by the differences between the DSM and the DEM. Note that CHMs and the corresponding DEMs and DSMs were produced at two different resolutions (1 m and 20 m). The 1 m-resolution CHMs were

used to generate CC products (in 20 m resolution) using a CHM-based method that showed a good correspondence with field measurements (Lucas et al. 2006). Each of 1 m × 1 m CHM cell with a value above a selected height threshold was coded as 1. A height threshold of 2 m was selected in this study to generate equivalent CC estimations from ALS data with the field measurements. The CC was calculated by the percentage of the number of coded CHM cells within each 20 m × 20 m grid. The accuracy of the ALS-derived pre- and post-treatment CC products was evaluated by the pre- and post-treatment field measurements, respectively.

The obtained 20 m-resolution CHMs and CCs were then used in the following FT detection procedures. The differences between the pre- and post-treatment CHMs and CCs were used to represent changes in forest structure, respectively. Because mechanical forest thinning, the main FT type conducted in the study area, usually incorporated the removal of vegetation to reduce the forest fuel load, CHM and CC were expected to have a drop in treated areas compared with control areas.

2.4. *High-resolution aerial imagery*

Aerial imagery (1 m resolution) from the National Agriculture Imagery Program (NAIP) was used in this study for the purpose of comparing the capability of ALS data on FT detection with that of traditional passive remote-sensing data. The 2005 colour-infrared (CIR) imagery (composed of green band, red band, and near-infrared (NIR) band) was used to represent the pretreatment forest, and the 2012 CIR imagery was selected to represent the post-treatment forest. Both pre- and post-treatment NAIP data were resampled to a resolution of 20 m using the weighted mean value method to obtain comparable results with field measurements. The misalignment of digital number (DN) values for time-invariant objects is one of the major error sources for applying change detection techniques on multi-temporal aerial images (Canty and Nielsen 2008; Lu et al. 2004; Singh 1989), and therefore radiometric normalization is one of the prerequisites for performing change detection algorithms on multi-temporal aerial images. To comprehensively compare the FT accuracy from aerial imagery with that from ALS data, two different techniques [normalized difference vegetation index (NDVI) differencing and standardized PCA] were applied to obtain change images from multi-temporal aerial imagery.

2.4.1. *Radiometric normalization*

We used an automatic iteratively re-weighted Multivariate Alteration Detection (IR-MAD) transformation method developed by Canty and Nielsen (2008) to determine the time-invariant pixels. These time-invariant pixels were then used to normalize the pre- and post-treatment aerial images. The IR-MAD method can calculate the no-change probability of pixels by transforming multi-temporal images into a set of mutually orthogonal difference images (Nielsen 2007). Only the pixels with no-change probability above the selected threshold (0.95 is a commonly used threshold) were selected as time-invariant pixels. In this study, the pretreatment aerial image was used as the reference image in the radiometric normalization procedure, and the post-treatment aerial image was used as the target image that needed to be normalized. Overall, 1,071 time-invariant pixels were selected. Two-thirds of them (714 pixels) were used as training pixels to normalize

the aerial images, and the remaining 357 pixels were saved to be used as testing pixels. It should be noted that all of the procedures described next related to aerial images were processed based on the radiometrically normalized aerial images.

2.4.2. *NDVI differencing method*

NDVI is one of most robust and frequently used vegetation indices in monitoring vegetation status and estimating vegetation parameters (Anyamba and Tucker 2005; Carlson and Ripley 1997; Carreiras, Pereira, and Pereira 2006; Pettorelli et al. 2005), which is defined as follows:

$$\mathrm{NDVI} = \frac{(\mathrm{DN})_{\mathrm{NIR}} - (\mathrm{DN})_{\mathrm{R}}}{(\mathrm{DN})_{\mathrm{NIR}} + (\mathrm{DN})_{\mathrm{R}}}, \tag{1}$$

where $\mathrm{DN}_{\mathrm{NIR}}$ and DN_{R} are the DN values in the NIR band and the red band, respectively. In this study, the pre- and post-treatment NDVI were calculated from the normalized aerial images, and the change image was represented by the difference between the pre- and post-treatment NDVI.

2.4.3. *Standardized PCA method*

Standardized PCA, one type of PCA algorithm, requires all input parameters to be standardized before performing the PCA algorithm. Eastman and Filk (1993) and Mas (1999) found that it is better for statistical control than the non-standardized PCA method and can improve the accuracy of change detection. Thus, in this study, all the six bands from normalized pre- and post-treatment aerial images were first standardized by the following equation:

$$\mathrm{DN}_{\mathrm{std}} = \frac{(\mathrm{DN})_{\mathrm{norm}} \quad \bar{x}}{\sigma}, \tag{2}$$

where $\mathrm{DN}_{\mathrm{std}}$ is the standardized DN values, $\mathrm{DN}_{\mathrm{norm}}$ is the original normalized DN values, and $\bar{x}$ and σ are the mean and standard deviation of the corresponding band, respectively. Then, both standardized pre- and post-treatment aerial images were used as the input for PCA transformations. In the standardized PCA routine outputs, the component having the poorest correlation with other components usually highlights the changed information, and therefore was selected as the change image. As shown in Table 1, in each row (or column), the R^2 for the relationship between the component represented by that row (or column) and component 4 is the smallest when related to all other components. Therefore, component 4 was selected to be used as the change image for the standardized PCA method in the FT detection routine described next.

Table 1. Correlations (represented by the R^2) between six components obtained from the standardized principal component analysis (PCA) for normalized pre- and post-treatment aerial images.

	Component 1	Component 2	Component 3	Component 4	Component 5	Component 6
Component 1	1.00	0.85	0.93	0.20	0.34	0.36
Component 2	0.85	1.00	0.98	0.07	0.64	0.62
Component 3	0.93	0.98	1.00	0.14	0.55	0.56
Component 4	0.20	0.07	0.14	1.00	0.07	0.27
Component 5	0.34	0.64	0.55	0.07	1.00	0.97
Component 6	0.36	0.62	0.56	0.27	0.97	1.00

3. FT detection methods

3.1. *FT detection strategy*

The same FT detection routine, combining pixel-wise thresholding and OBI segmentation, was applied to the above-mentioned change images (Figure 2). An unfiltered pixel-wise FT result was first obtained by using a threshold to differentiate treated and untreated pixels in the change image. In this study, we assumed that the change parameter should be normally distributed, and the variation within the 95% confidence should be recognized as the background information. Thus, $\mu \pm 1.96\sigma$ was used as the threshold to differentiate the treated and untreated pixels, where μ and σ are the mean and standard deviation of the change image, respectively. It should be noted that the threshold was only selected at one side (either $\mu + 1.96\sigma$ or μ–1.96σ) because FTs only remove trees and can only result in unidirectional movement of the selected change parameters.

However, we anticipated that noise would still remain in the unfiltered pixel-wise results. To further remove the noise, the OBI segmentation method was used to filter the pixel-wise result considering the fact that FTs were usually conducted in spatially continuous areas (Zhang, Xiao, and Feng 2013). The OBI segmentation was conducted using the 'Segment Only Feature Extraction Workflow' module in Exelis Environment Visual Information (ENVI) software. The mean of a change image within each segmented polygon was then used to determine its treatment attribute. If its value exceeded the threshold (μ +/- 1.96σ) used in the pixel-wise thresholding procedure, this polygon was recognized as treated, and vice versa. The identified isolated treated polygons with an

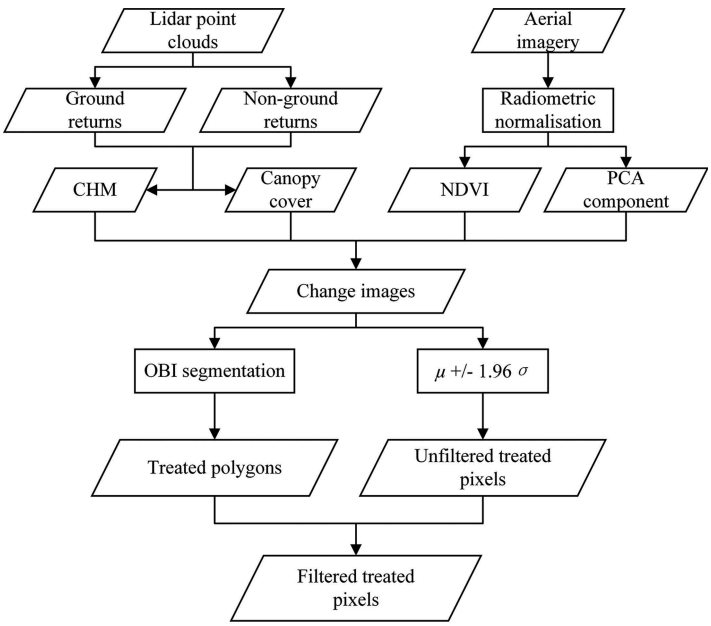

Figure 2. The procedure for forest treatment detection that combines a pixel-wise threshold control method and an object-of-interest segmentation method. Note that μ and σ are the mean and standard deviation of the change image, respectively.

area smaller than 800 m^2 were further removed in the OBI segmentation workflow. Finally, the detected unfiltered FT pixels within the retained treated polygons were recognized as the final pixel-wise FT extents.

3.2. *FT intensity recognition*

Within the detected FT extents from the method producing the highest accuracy, we further developed and tested a method to identify the FT intensity directly from multi-temporal ALS point clouds. We hypothesized that FT activities can change the vertical structure of forests and therefore influence the vertical distribution of ALS points. Therefore, we chose the vertical profile area change between the pre- and post-treatment ALS points within a pixel to represent the FT intensity. The profile area change can be calculated from pre- and post-treatment raw ALS point clouds using the following procedure. (1) Normalize the height of raw ALS points using DEM. (2) Normalize the height of ALS points from Step 1 to 0–1 within each 20 m × 20 m cell. This aimed at reducing the influence of different vegetation heights on the FT intensity recognition result. (3) Sort all ALS points from Step 2 within each 20 m × 20 m pixel ascendingly by height, and draw a height percentile ranking profile for each pixel (Figure 3). (4) Compute the area composed by the percentile ranking profile and the *x*-axis (i.e. the axis labelled as Point Count in Figure 3) for each 20 m × 20 m cell. (5) Calculate the profile area change as the difference between the profile areas of post- and pretreatment ALS point clouds (i.e. the highlighted grey zones in Figure 3).

The profile area change can range from −100% to 100%, theoretically. When a pixel contains no trees in the pretreatment condition but the post-treatment condition has dense enough trees that prevent the ALS signal from penetrating the forest canopy, its profile area change should be −100%. Conversely, if a pixel contains dense trees in the pretreatment condition but all are cut down by FT activities, then the profile area change should be 100%. If there are no FT activities in a pixel, the corresponding profile area should be very similar and the profile area change should be close to 0%. Figure 3 shows two typical examples (i.e. with and without FT) in the study area. As shown in

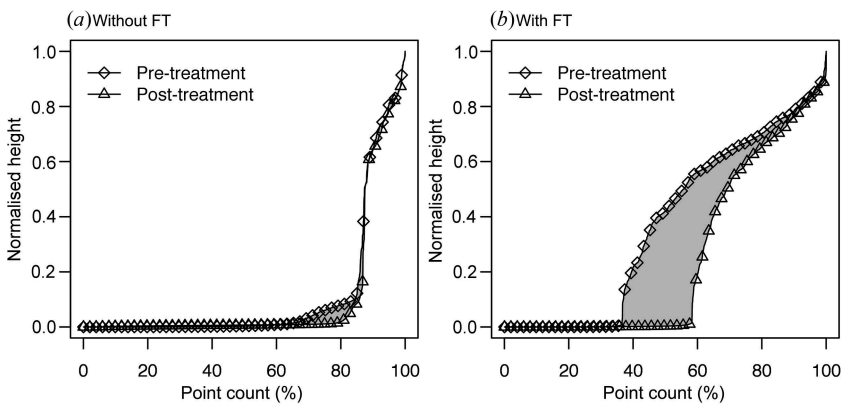

Figure 3. Examples of pre- and post-treatment percentile ranking profiles (*a*) in a 20 m × 20 m pixel that has not been treated, and (*b*) in a 20 m × 20 m pixel that has been treated.

Figure 3(*a*), for a pixel without FT, the pre- and post-treatment profiles are almost identical, and the slight tree growth during the time span of the two ALS flights results in a small negative profile area change (–0.95% for Figure 3(*a*)). In a pixel with FT (Figure 3(*b*)), the number of post-treatment ALS points in upper height levels is significantly increased and the number in lower height levels can be decreased. These changes can lead to a relatively large positive profile area change (11.94% for Figure 3 (*b*)), and the higher the profile area change is, the higher the FT intensity should be.

3.3. *Accuracy assessment*

Polygons from the USFS that illustrate the intended FT boundary were used to compare with FT detection results of the different methods. The proportions of the detected FT areas within the USFS treatment footprints were calculated for all FT detection results. Additionally, plot measurements were also used to evaluate the FT detection accuracy by the total accuracy (τ) and kappa coefficient (κ), which can be denoted as

$$\tau = \frac{a}{N}, \tag{3}$$

$$\kappa = \frac{p_o \quad p_e}{1 \quad p_e}, \tag{4}$$

where a is the number of plots agreeing with the FT detection result, and N is the total number of plots; p_o is the relative observed agreement, and p_e is the hypothetical probability of chance agreement (Jensen 2005). It should be noted that a 20 m-radius buffer was made for each plot to compare with the FT detection result considering the influence of plot size and the mis-registration between the plots and ALS data and aerial images. If the plot was labelled as treated in the field, it would be recognized as true positive (correctly identified by FT detection results) when any part of its buffer overlapped with a treated pixel from FT detection results; otherwise, it would be recognized as false positive (incorrectly identified by FT detection results). If the plot was labelled as untreated in the field, it would be recognized as true negative (correctly rejected by FT detection results) when its buffer was isolated from the treated pixels from the FT detection results; otherwise, it would be recognized as false negative (incorrectly rejected by FT results).

4. Results

4.1. *ALS-derived CC*

Both pre- and post-treatment CCs were positively correlated with the field measurements (Figure 4). The coefficients of determination (R^2) for the correlations between both pre- and post-treatment ALS-derived CC and field measurements are above 0.5. The R^2 for the post-treatment correlation is slightly higher than that for the pretreatment correlation. The mean difference between the pretreatment ALS-derived CC and field measurements is 13.7%, and that for the post-treatment is 5.5%. The absolute value of coefficient of variation of the root mean square error (CV(RMSE)) for the pretreatment is slightly lower than that for the post-treatment. Figure 5 shows the change in CC

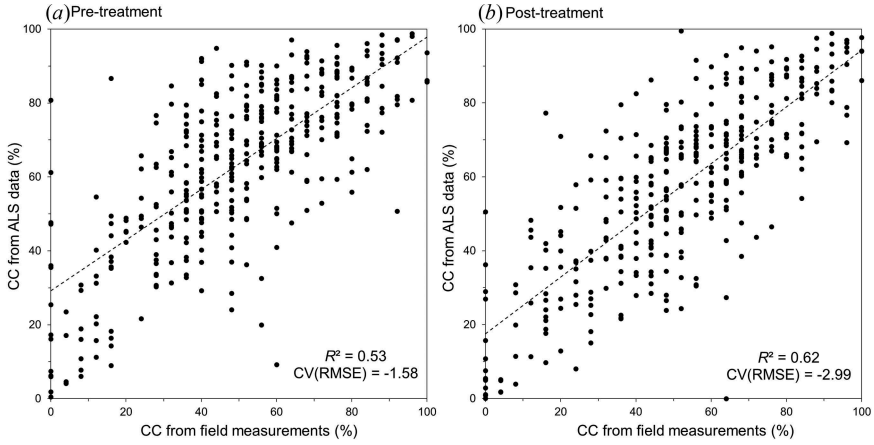

Figure 4. Comparison between the ALS-derived canopy cover (CC) and field-measured CC for both (*a*) pretreatment and (*b*) post-treatment. R^2 represents the coefficient of determination, and CV (RMSE) represents the coefficient of variation of the root mean square error.

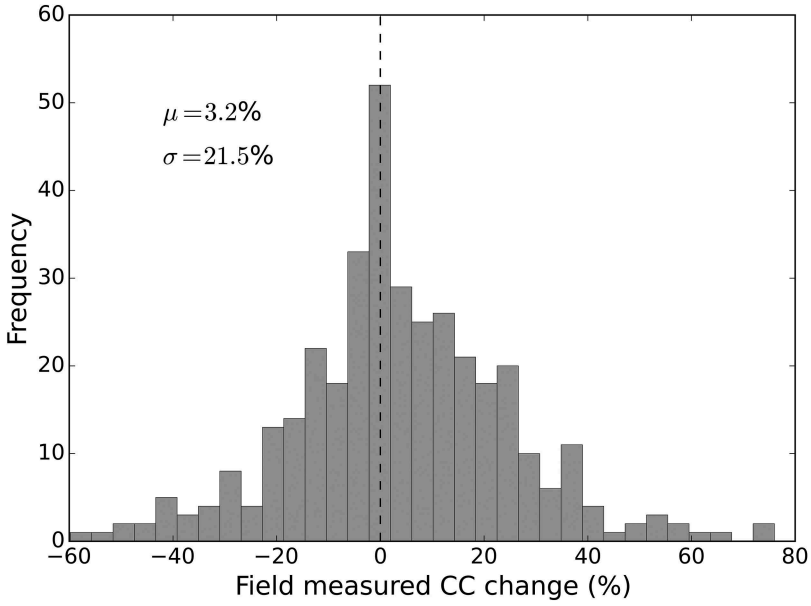

Figure 5. Histogram of changes between pre- and post-treatment field-measured CC (post-treatment CC minus pretreatment CC). μ represents the mean difference, and σ represents the standard deviation.

observed from the field measurements. In general, the study area has a 3% increase in CC. However, the changed area is widely distributed from −60% to 80%.

Both pre- and post-treatment ALS-derived CCs are systematically higher than the field measurements. More than 83% and 63% of the pre- and post-treatment ALS-derived CCs are higher than the pre- and post-treatment field measurements, respectively. This result is expected since the sight tube can recognize a finer canopy gap than the CHM method

Table 2. The comparison between the field-measured canopy cover (CC) and ALS-derived CC for plots that were identified as treated areas in the field but with an increase in field-measured CC.

	Field-measured CC (%)			ALS-derived CC (%)		
Plot ID	Pretreatment	Post-treatment	Post-Pre*	Pretreatment	Post-treatment	Post-Pre*
109	48	56	8	65.1	53.7	−11.4
131	32	68	36	84.7	81.7	−3.0
216	60	64	4	51.6	62.6	11.0
224	48	56	8	51.0	30.5	−20.5
233	52	60	8	78.1	61.2	−16.9
242	56	60	4	68.3	55.0	−13.2
266	24	32	8	62.2	54.6	−7.6
281	28	32	4	33.7	29.9	−3.8
283	20	36	16	45.3	40.67	−4.7
322	36	48	12	72.6	54.8	−17.8
337	40	52	12	71.3	57.9	−13.4
354	52	64	12	57.0	53.7	−3.3

*'Post-Pre' means using the post-treatment CC minus the pretreatment CC.

used in this study. Besides, the ALS-derived CC may be more consistent than the field measurements. FTs usually involve the selective removal of trees, which can result in a decrease in CC. However, based on field measurements, there are 12 out of 46 treated plots with an increase in CC. Eleven of these plots showed a drop in CC from ALS data, and only one has an increase in CC (Table 2). This phenomenon might have resulted from the insufficient sampling points to measure the CC in the field. Studies have found that the CC obtained using a sight tube with 23 points had a 5.5% underestimation compared with the CC using 195 points (Korhonen et al. 2006), and might be insufficient to capture the variation in forest canopy (Fiala, Garman, and Gray 2006).

4.2. *Radiometric normalization for aerial images*

The built radiometric normalization equation for each band using the IR-MAD method is shown in Figure 6. The R^2 for the green and red bands are both higher than 0.9, and that for the NIR band is slightly lower. The accuracy assessment by the 357 time-invariant testing pixels is listed in Table 3. The differences of means and variances between the normalized post- and pretreatment aerial images are 98% and 70% smaller than those between the original post- and pretreatment aerial images on average, respectively. Moreover, the p-values for the test of equal means and variances between the pretreatment aerial image and the normalized post-treatment aerial image are higher than the significance level of $\alpha = 0.05$, which indicates that means and variances between the pretreatment aerial image and the normalized post-treatment aerial image have no significant differences.

4.3. *FT detection results*

The unfiltered pixel-wise FT detection results are shown in Figure 7. To quantitatively describe the noise rate, the detected FT areas outside the USFS FT footprints are temporally considered as 'noise', and the noise rate is defined as the ratio of 'noise' area to all detected FT area. As can be seen, the noise rate for the FT detection result using CC from ALS data is the lowest at 37%. The noise rates using CHM from ALS data and NDVI and standardized PCA methods from aerial imagery are slightly higher at 41%, 51%, and 41%, respectively.

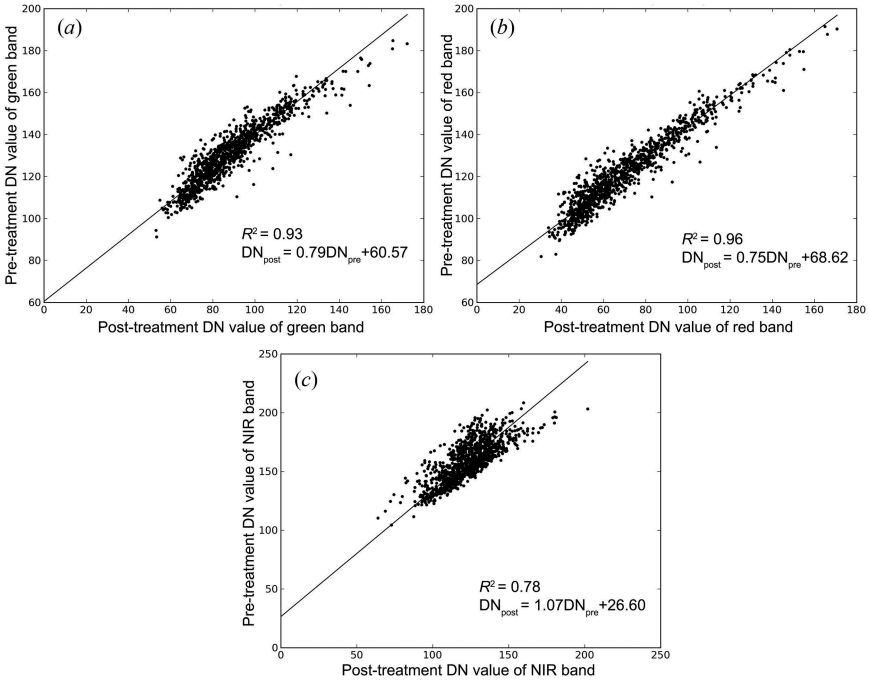

Figure 6. Scatter plots for the 714 time-invariant training pixels obtained from IR-MAD normalization method and the corresponding simulated radiometric normalization equations for (*a*) green band, (*b*) red band, and (*c*) near infrared (NIR) band of aerial images.

Table 3. Comparison of means and variances for the 357 time-invariant testing pixels of pretreatment, post-treatment, and normalized post-treatment aerial images. Paired *t*-test and *F*-test were used to test equal means and variances between the pretreatment aerial image and the normalized post-treatment aerial image.

Variables	Green band	Red band	NIR band
Pretreatment mean	130.6	121.3	158.9
Post-treatment mean	87.6	69.4	123.9
Normalized post-treatment mean	130.1	120.8	159.8
p-value (paired *t*-test) for means	0.15	0.12	0.11
Pretreatment variance	211.0	311.1	304.0
Post-treatment variance	290.3	510.9	293.9
Normalized post-treatment variance	182.9	288.6	339.1
p-value (*F*-test) for variances	0.18	0.48	0.30

After applying the OBI segmentation routine to filter the pixel-wise results, the noise rate for all FT detection results was found to have a significant decrease (Figure 8). Most of the noise from the ALS-derived CC method and the aerial image-derived NDVI method are concentrated in the northeastern and southwestern areas, and most of the noise from the standardized PCA method are concentrated in the southwestern areas.

The accuracy of the FT detection method was further assessed by plot measurements. The FT detection using the ALS-derived CC showed the highest accuracy among all the results. The total accuracy for the FT detection result using ALS-derived CC is about an average of 4% higher than the other three methods, and the κ is about an average of 23%

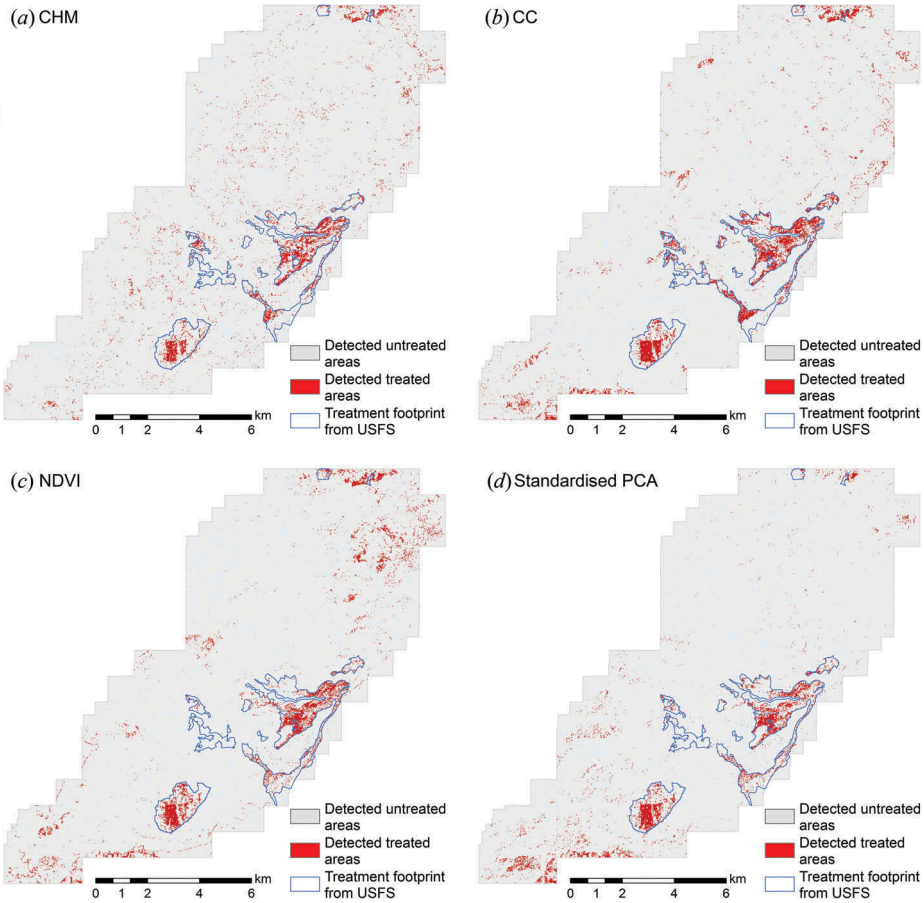

Figure 7. Unfiltered pixel-wise FT detection results from the methods using (*a*) ALS-derived canopy height model (CHM), (*b*) ALS-derived CC, (*c*) aerial imagery-derived normalized difference vegetation index (NDVI), and (*d*) aerial imagery-derived standardized principle component analysis (PCA) change component. The location of the study site is presented in Figure 1.

higher (Table 4). This is further supported by its producer accuracy, defined as the percentage of correct predictions based on field measurements. Its producer accuracy for the treated areas is 74%, compared with 59%, 63%, and 70% for the CHM method, the NDVI method, and the standardized PCA method, respectively; its producer accuracy for the untreated areas is about 96%, compared with 96%, 94%, and 92% for the other three methods, respectively (Table 3). Moreover, it accurately identified the FT activity in the USFS FT footprints within the rectangles 'A', 'B', 'C', and 'D' in Figure 8. All the other three methods detected close to nothing from these areas, except the CHM method within the rectangle 'A' (Figure 8(*a*)). The area within rectangle 'E' in Figure 8 was only recognized as treated by the method using the ALS-derived CC. This area may have true FT detection for the fact that there were plots recognized as treated in it.

The CHM method from ALS data has slightly better accuracy than the NDVI method and the standardized PCA method using aerial images. Both total accuracy and κ using the ALS-derived CHM method are higher than the two methods using aerial images. The

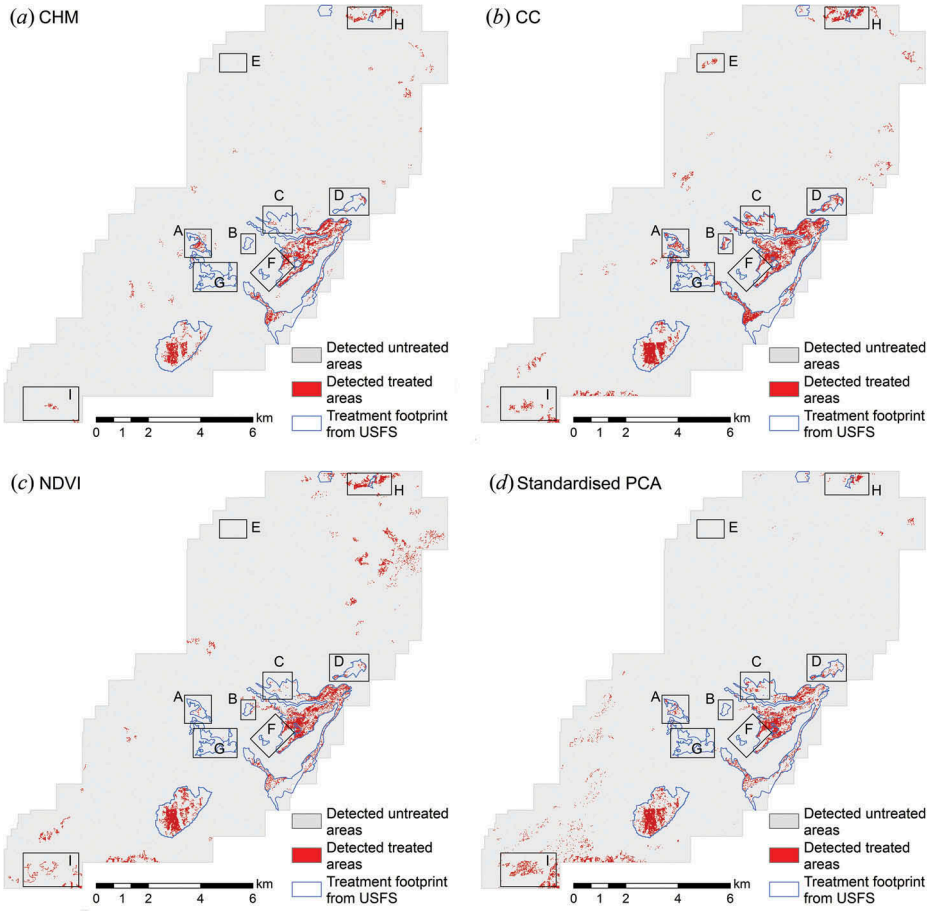

Figure 8. Filtered pixel-wise FT detection results from the methods using (*a*) ALS-derived CHM, (*b*) ALS-derived CC, (*c*) aerial imagery-derived NDVI, and (*d*) aerial imagery-derived standardized PCA change component. Areas in black rectangles marked with 'A'–'H' are examples for different scenarios. Area 'A' can be identified by methods using lidar data but not methods using aerial imagery; area 'B' to area 'D' can only be identified by the lidar-derived CC method; area 'E', area 'H', and area 'I' can be identified by at least one of the four FT detection methods used in this study, but are not within the USFS FT footprints; area 'F' and area 'G' are within the USFS FT footprints, but cannot be identified by any of the four FT detection methods. The location of the study site is presented in Figure 1.

two methods using aerial images provided similar accuracies. Although the total accuracy for the result using the NDVI method is higher than that using the standardized PCA method and its κ is lower, their differences are extremely small, which are only 0.27% and 0.01, respectively (Table 4).

4.4. *FT intensity distribution*

As mentioned in Section 4.3, the ALS-derived CC produced the FT detection result with the highest accuracy. Therefore, we tested the proposed FT intensity recognition method based on the FT extents from ALS-derived CC. Figure 9 shows the distribution

Table 4. Forest treatment detection accuracy assessment by comparing with field plot measurements.

		CHM		CC		NDVI*		Standardized PCA	
		Treated	Non-treated	Treated	Non-treated	Treated	Non-treated	Treated	Non-treated
Field data	Treated	27	19	34	12	29	17	32	14
	Non-treated	12	311	12	311	21	302	25	298
Total accuracy (%)		91.6		93.5		89.7		89.4	
Kappa coefficient		0.59		0.70		0.55		0.56	

*Normalized difference vegetation index.

of profile area changes (pretreatment minus post-treatment) within the FT extents. All profile area changes within the FT extents are larger than 0% (Figure 9). The intensity of FTs conducted in the southern part of the study area is relatively larger, where the profile area change is over 20% in general. The profile area changes of FTs conducted in the middle and northern parts of the study area are concentrated in values from 5% to 20%. Based on our plot measurements, the only two plots labelled as cable thinning in

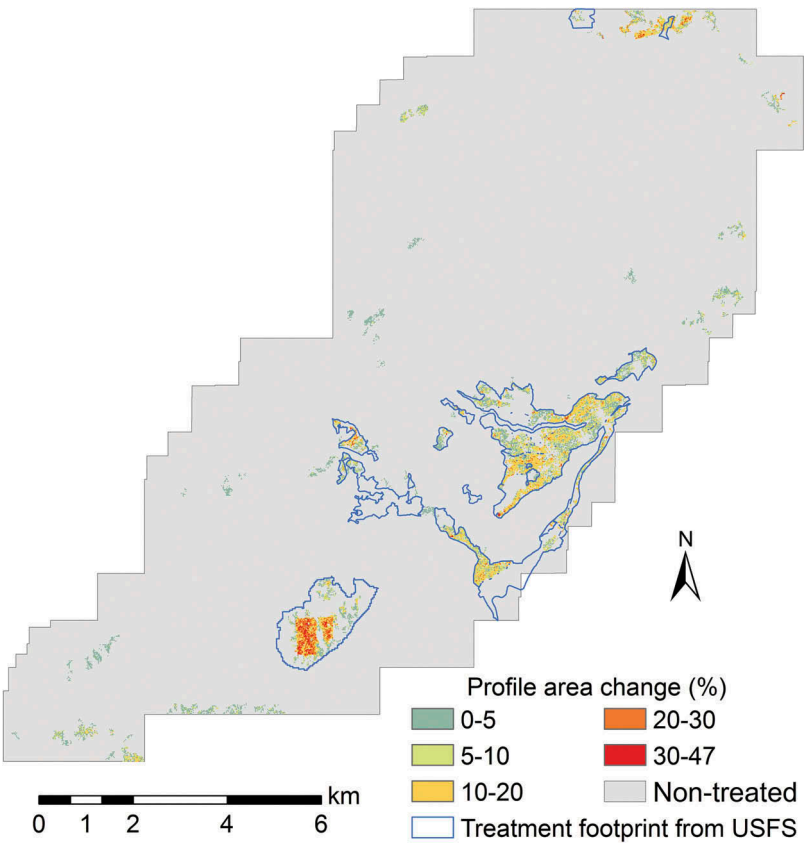

Figure 9. The FT intensity distribution of the study area indicated by the profile area change in each 20 m × 20 m pixel (pretreatment profile area minus post-treatment profile area). Note that this result is based on the FT detection result using the lidar-derived CC method, which has the highest detection accuracy. The location of the study site is presented in Figure 1.

the field (indicating the removal of big trees) have profile area change values larger than 15%, and the only two plots labelled as mastication (indicating the removal of surface fuels, e.g. bushes) have profile area change values between 3% and 5%. Regarding the other 42 treated plots, they were labelled as general forest thinning, and therefore we cannot perform a detailed evaluation on the FT intensity recognition result currently.

5. Discussion

In this study, we compared our FT detection results with other published works on using change detection techniques to monitor forest changes or map wildfires, and the accuracies of the FT detection results from all four methods in this study are comparable to these studies. For example, Desclée, Bogaert, and Defourny (2006) monitored the land-cover changes including forested areas in Eastern Belgium from Satellite Pour l'Observation de la Terre-High Resolution Visible (SPOT-HRV) imagery using a statistical OBI method and obtained an accuracy of over 90%; Kennedy, Cohen, and Schroeder (2007) detected forest disturbance dynamics in western Oregon, US, from Landsat TM imagery using a trajectory-based change detection method and obtained an overall accuracy of 90%; Schroeder et al. (2011) mapped wildfire and clear-cut harvest disturbances from Landsat TM imagery in central Saskatchewan and obtained a total accuracy of around 90%. In this study, the total accuracies of the results of all four methods can reach approximately 90%, which are similar to the values of these studies.

Among the four FT detection methods in this study, the FT detection results from the ALS-derived CC method achieved the highest accuracy. A possible explanation for this may be related to the possible superiority of the ALS-derived CC method in identifying less-intensive FTs. Examining an example in areas within rectangle 'B' in Figure 8, nearly all removed trees in this area were short-statured trees (usually lower than 5 m in height) and were dispersed. We can clearly see that the removal of these small trees can still lead to a decrease in CC (Figure 10(*a*,*b*)), which may increase the possibility for the ALS-derived CC method to effectively detect these FT areas. Moreover, this result is also in agreement with other previously published works. Stephens et al. (2009) found that the CC decreased significantly in forests with mechanical FTs, and Kramer et al. (2014) found that the lidar percentage cover between 2 and 4 m was strongly correlated to the forest ladder fuels and could be used to differentiate treated areas from untreated areas. To examine the influence of different height cut-offs on the FT detection results, we performed the same FT detection routine using the ALS-derived CC products at 5 m and 10 m cut-offs, respectively (Figure 11). The omission rate of the results using a 5 m cut-off was only increased by around 8% compared with the results using a 2 m cut-off. After the cut-off reached 5 m, the omission rate increased rapidly, and the omission rate of the results using a 10 m cut-off was 100%.

The accuracy of FT detection from methods using aerial imagery (NDVI and standardized PCA) is generally lower than methods using ALS data. Both of these two methods poorly detected areas with less-severe FTs. As mentioned, due to the penetration limitation, the aerial images can reflect the forest surface spectral characteristics, but may not provide accurate forest structure information (Weishampel et al. 2000). This is particularly problematic for detecting change in areas where overstorey trees are unaffected, which is common for most FTs (Agee and Skinner 2005). Moreover, both of these two methods

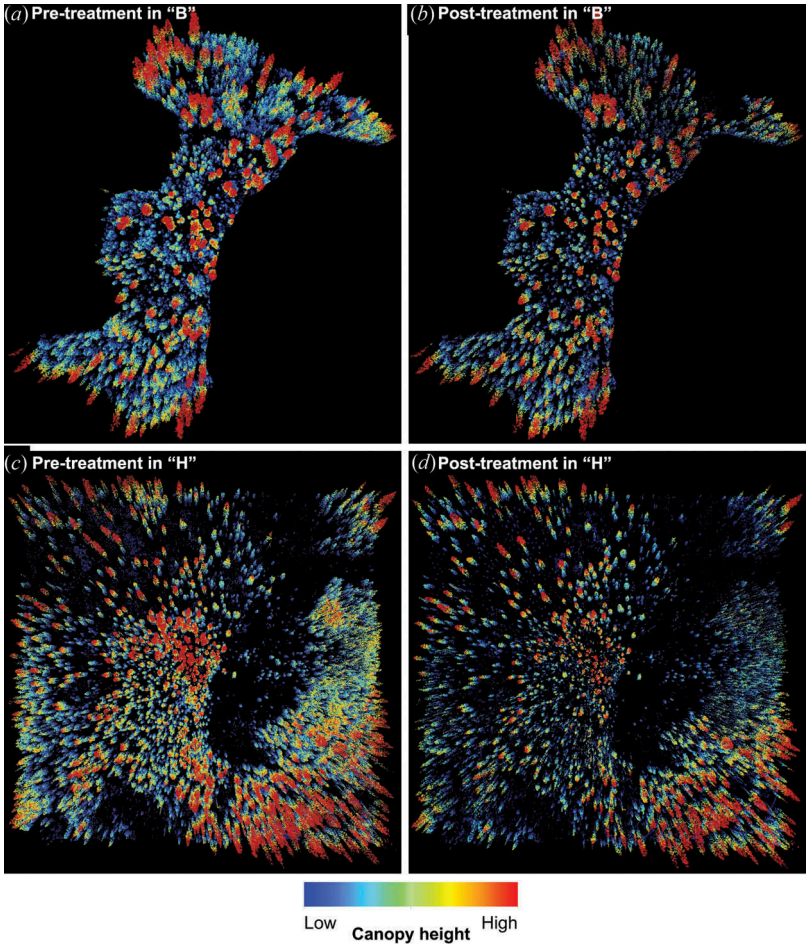

Figure 10. Comparison between the pre- and post-treatment three-dimensional point clouds within the rectangle 'B' ((*a*) and (*b*)) and the rectangle 'H' ((*c*) and (*d*)) in Figure 8.

using aerial imagery have relatively high false FT detection rates, which are located at the northeast and southwest of the study area, respectively. The high false detection effects were commonly observed in previous studies using NDVI to map forest fires (Remmel and Perera 2001). One of the possible explanations is the light cloud contamination suppressed the NDVI (Remmel and Perera 2001). Another possible reason may be related to the tree mortality in those areas, which can result in a significant change in forest surface spectral reflectance (Jensen 2005; Liu, Kelly, and Gong 2006). Dead trees, especially those far away from the road (greater than 60 m), may not be removed from the forest.

Among the so-called noise areas, there are some common areas that were detected by several methods, which are concentrated in the north of the study site (within the rectangle 'H') and the south of the study site (within the rectangle 'I') (Figure 8). Although these areas are not included in the USFS FT footprints, this may not mean that these areas have not been treated. Figure 10(*c*,*d*) shows the comparison between the pre- and post-treatment point clouds in the sub-area within rectangle 'H'. It can clearly be seen that there are trees

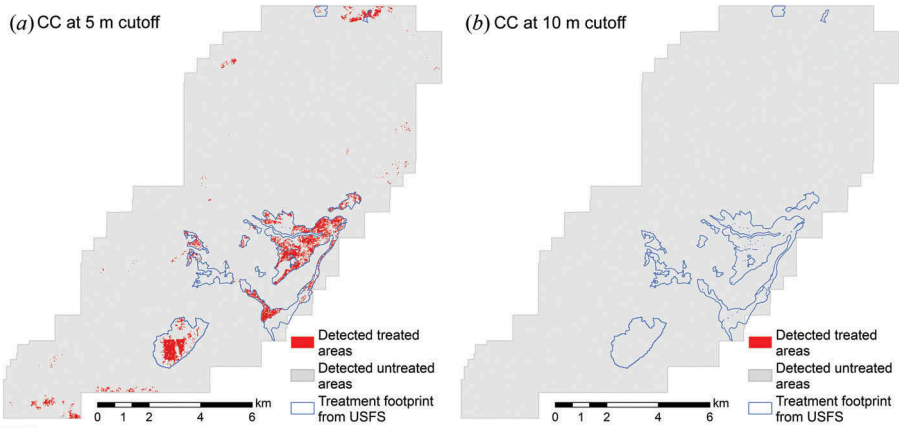

Figure 11. Comparison between FT detection results using the ALS-derived CC products computed at height breaks of (*a*) 5 m and (*b*) 10 m, respectively.

that have been removed, suggesting that this area might have been treated. There are some areas within the USFS FT footprints but cannot be detected by any of the four methods, e.g. areas within rectangles 'F' and 'G' in Figure 8. It is possible that in these areas the intact overstorey trees, which were not removed in the FTs, obstructed our ability to detect the removal of small tress with both ALS data and aerial imagery. There are eight field plots within the USFS FT footprints under these two squares, and six of them were identified as non-treated in the field. Even for ALS data, the capability for mapping understorey shrubs in dense forest stands can be limited (Estornell et al. 2011; Hodgson et al. 2005; Jakubowksi et al. 2013).

The proposed FT intensity recognition method shows the potential to detect the conducted FT types by comparing with a limited number of field measurements. As mentioned, Kramer et al. (2014) found that the lidar percentage cover between 2 and 4 m was highly correlated with forest ladder fuels. However, the height breaks or strata may not be consistent for different areas or treatment types. The proposed method directly examines the change in the vertical distribution of ALS point clouds, and may be applicable in different areas. Unfortunately, owing to the lack of detailed ground truth data, we cannot map different profile area change values to different FT types in the current study. Moreover, different point cloud densities of different ALS flights may also influence the value of the profile area change. In this study, the pre- and post-treatment ALS data were acquired using the same protocol, and were accurately co-registered together using ground control points. This made the point cloud densities of the pre- and post-treatment flights very close. However, in most cases, the ALS point density from different ALS flights may significantly differ from each other. Further study is still needed to identify how different ALS point densities influence the profile area changes.

Recently, the cost of ALS data acquisition has decreased (Tilley et al. 2004) and is comparable to or even less expensive than the cost of large-scale field data collection and image data analysis (Hummel et al. 2011; Jakubowski, Guo, and Kelly 2013). For example, Hummel et al. (2011) compared the cost of using ALS data to examine forest structural attributes with the cost of using field measurements, and found that the cost

of ALS data (6.31 points/m^2) acquisition and process was $2.63/ac (acre) (US dollar) compared with $2.46/ac (US dollar) to collect field measurements. Johansen, Phinn, and Witte (2010) evaluated the costs of using ALS data (3.98 point/m^2), QuickBird imagery, and SPOT-5 imagery to study a stream network with a length of 26,000 km, and the total research costs using these three data sets were $3.8 M, $6.4 M, and $2.6 M (Australian dollar), respectively. Besides, considering the improvement of using ALS-derived CC products to detect FTs (an increase of around 23% in κ compared with the methods using aerial imagery) and the capability of ALS data on mapping the FT intensity, it may be a better choice for forest managers to use ALS data to manage FT activities.

6. Conclusions

This study developed a method combing pixel-wise thresholding and OBI segmentation to identify FT extents from ALS-derived CC and CHM. A systematic comparison using the same FT detection routine as using ALS data was made to evaluate the capability of ALS data and aerial imagery on detecting FT extents. The results demonstrate the ability of ALS data to penetrate forest canopy, making it a more effective tool than aerial imagery for capturing forest structure change following FTs. Both ALS-derived CHM and CC provided higher accuracy in their FT detection results. The ALS-derived CC, which can reflect the vertical structure information of a forest, produced an even better result than the ALS-derived CHM method. Its total detection accuracy is over 93%, and its κ is 0.7, both of which are the highest among all the methods. FT detection results using NDVI and standardized PCA from multi-temporal aerial imagery produced almost identical total accuracy and κ. Both methods showed relatively limited capacity to detect light FT areas, and had higher false detection rates (recognized untreated areas as treated areas) compared with the methods using ALS-derived parameters.

Moreover, this study developed and tested a method to detect FT intensity directly from ALS point clouds. Based on a limited number of plot measurements, the methods show great potential to identify different FT types. However, we cannot make a detailed evaluation on the result due to the lack of ground truth in the current study. Besides, the change of ALS point densities of different ALS flights still needs to be further studied.

Acknowledgements

This is SNAMP Publication Number 47. The Sierra Nevada Adaptive Management Project is funded by USDA Forest Service Region 5, USDA Forest Service Pacific Southwest Research Station, US Fish and Wildlife Service, California Department of Water Resources, California Department of Fish and Game, California Department of Forestry and Fire Protection, and the Sierra Nevada Conservancy. We thank USFS, Tahoe National Forest, American River District personnel for providing the FT boundaries. “Besides, this work is supported by the National Science Foundation [DBI 1356077] and National Science Foundation of China [project numbers 41471363 and 31270563].” We also thank Dr John J. Battles for helpful suggestions on the article.

Disclosure statement

No potential conflict of interest was reported by the authors.

References

Agee, J. K., and C. N. Skinner. 2005. "Basic Principles of Forest Fuel Reduction Treatments." *Forest Ecology and Management* 211 (1–2): 83–96. doi:10.1016/j.foreco.2005.01.034.

Allen, T. R., and J. A. Kupfer. 2000. "Application of Spherical Statistics to Change Vector Analysis of Landsat Data: Southern Appalachian Spruce-Fir Forests." *Remote Sensing of Environment* 74 (3): 482–493. doi:10.1016/S0034-4257(00)00140-1.

Andersen, H. E., R. J. McGaughey, and S. E. Reutebuch. 2005. "Estimating Forest Canopy Fuel Parameters Using LIDAR Data." *Remote Sensing of Environment* 94 (4): 441–449. doi:10.1016/j.rse.2004.10.013.

Anyamba, A., and C. Tucker. 2005. "Analysis of Sahelian Vegetation Dynamics Using NOAA-AVHRR NDVI Data from 1981–2003." *Journal of Arid Environments* 63 (3): 596–614. doi:10.1016/j.jaridenv.2005.03.007.

Bortolot, Z. J., and R. H. Wynne. 2005. "Estimating Forest Biomass Using Small Footprint Lidar Data: An Individual Tree-Based Approach that Incorporates Training Data." *ISPRS Journal of Photogrammetry and Remote Sensing* 59 (6): 342–360. doi:10.1016/j.isprsjprs.2005.07.001.

Canty, M. J., and A. A. Nielsen. 2008. "Automatic Radiometric Normalization of Multitemporal Satellite Imagery with the Iteratively Re-Weighted MAD Transformation." *Remote Sensing of Environment* 112 (3): 1025–1036. doi:10.1016/j.rse.2007.07.013.

Carlson, T. N., and D. A. Ripley. 1997. "On the Relation between NDVI, Fractional Vegetation Cover, and Leaf Area Index." *Remote Sensing of Environment* 62 (3): 241–252. doi:10.1016/S0034-4257(97)00104-1.

Carreiras, J., J. Pereira, and J. S. Pereira. 2006. "Estimation of Tree Canopy Cover in Evergreen Oak Woodlands Using Remote Sensing." *Forest Ecology and Management* 223 (1–3): 45–53. doi:10.1016/j.foreco.2005.10.056.

Clark, M. L., D. B. Clark, and D. A. Roberts. 2004. "Small-Footprint Lidar Estimation of Sub-Canopy Elevation and Tree Height in a Tropical Rain Forest Landscape." *Remote Sensing of Environment* 91 (1): 68–89. doi:10.1016/j.rse.2004.02.008.

Collins, B. M., S. L. Stephens, J. J. Moghaddas, and J. Battles. 2010. "Challenges and Approaches in Planning Fuel Treatments across Fire-Excluded Forested Landscapes." *Journal of Forestry* 108 (1): 24–31.

Collins, B. M., S. L. Stephens, G. B. Roller, and J. J. Battles. 2011. "Simulating Fire and Forest Dynamics for a Landscape Fuel Treatment Project in the Sierra Nevada." *Forest Science* 57 (2): 77–88.

Collins, J. B., and C. E. Woodcock. 1994. "Change Detection Using the Gramm-Schmidt Transformation Applied to Mapping Forest Mortality." *Remote Sensing of Environment* 50 (3): 267–279. doi:10.1016/0034-4257(94)90076-0.

Collins, J. B., and C. E. Woodcock. 1996. "An Assessment of Several Linear Change Detection Techniques for Mapping Forest Mortality Using Multitemporal Landsat TM Data." *Remote Sensing of Environment* 56 (1): 66–77. doi:10.1016/0034-4257(95)00233-2.

Desclée, B., P. Bogaert, and P. Defourny. 2006. "Forest Change Detection by Statistical Object-Based Method." *Remote Sensing of Environment* 102 (1–2): 1–11. doi:10.1016/j.rse.2006.01.013.

Dubayah, R., S. Sheldon, D. Clark, M. Hofton, J. Blair, G. Hurtt, and R. Chazdon. 2010. "Estimation of Tropical Forest Height and Biomass Dynamics Using Lidar Remote Sensing at La Selva, Costa Rica." *Journal of Geophysical Research: Biogeosciences* 115 (G2). doi:10.1029/2009JG000933.

Eastman, J. R., and M. Filk. 1993. "Long Sequence Time Series Evaluation Using Standardized Principal Components." *Photogrammetric Engineering and Remote Sensing* 59 (6): 991–996.

Estornell, J., L. Ruiz, B. Velázquez-Martí, and A. Fernández-Sarría. 2011. "Estimation of Shrub Biomass by Airborne Lidar Data in Small Forest Stands." *Forest Ecology and Management* 262 (9): 1697–1703. doi:10.1016/j.foreco.2011.07.026.

Fiala, A. C. S., S. L. Garman, and A. N. Gray. 2006. "Comparison of Five Canopy Cover Estimation Techniques in the Western Oregon Cascades." *Forest Ecology and Management* 232 (1–3): 188–197. doi:10.1016/j.foreco.2006.05.069.

Guerra, F., H. Puig, and R. Chaume. 1998. "The Forest-Savanna Dynamics from Multi-Date Landsat-TM Data in Sierra Parima, Venezuela." *International Journal of Remote Sensing* 19 (11): 2061–2075. doi:10.1080/014311698214866.

Guo, Q., W. Li, H. Yu, and O. Alvarez. 2010. "Effects of Topographic Variability and Lidar Sampling Density on Several DEM Interpolation Methods." *Photogrammetric Engineering & Remote Sensing* 76 (6): 701–712. doi:10.14358/PERS.76.6.701.

Hame, T., I. Heiler, and J. San Miguel-Ayanz. 1998. "An Unsupervised Change Detection and Recognition System for Forestry." *International Journal of Remote Sensing* 19 (6): 1079–1099. doi:10.1080/014311698215612.

Hao, M., W. Z. Shi, H. Zhang, and C. Li. 2014. "Unsupervised Change Detection with Expectation-Maximization-Based Level Set." *IEEE Geoscience and Remote Sensing Letters* 11 (1): 210–214. doi:10.1109/LGRS.2013.2252879.

Hodgson, M. E., J. Jensen, G. Raber, J. Tullis, B. A. Davis, G. Thompson, and K. Schuckman. 2005. "An Evaluation of Lidar-Derived Elevation and Terrain Slope in Leaf-Off Conditions." *Photogrammetric Engineering & Remote Sensing* 71 (7): 817–823. doi:10.14358/PERS.71.7.817.

Hudak, A. T., M. A. Lefsky, W. B. Cohen, and M. Berterretche. 2002. "Integration of Lidar and Landsat ETM+ Data for Estimating and Mapping Forest Canopy Height." *Remote Sensing of Environment* 82 (2–3): 397–416. doi:10.1016/S0034-4257(02)00056-1.

Hummel, S., A. T. Hudak, E. H. Uebler, M. J. Falkowski, and K. A. Megown. 2011. "A Comparison of Accuracy and Cost of Lidar versus Stand Exam Data for Landscape Management on the Malheur National Forest." *Journal of Forestry* 109 (5): 267–273.

Jakubowksi, M. K., Q. Guo, B. Collins, S. Stephens, and M. Kelly. 2013. "Predicting Surface Fuel Models and Fuel Metrics Using Lidar and CIR Imagery in a Dense, Mountainous Forest." *Photogrammetric Engineering & Remote Sensing* 79 (1): 37–49. doi:10.14358/PERS.79.1.37.

Jakubowski, M. K., Q. Guo, and M. Kelly. 2013. "Tradeoffs between Lidar Pulse Density and Forest Measurement Accuracy." *Remote Sensing of Environment* 130 (3): 245–253. doi:10.1016/j.rse.2012.11.024.

Jensen, J. R. 2005. *Introductory Digital Image Processing. A Remote Sensing Perspective*. Upper Saddle River, NJ: Prentice Hall Series in Geographic Information Science.

Johansen, K., S. Phinn, and C. Witte. 2010. "Mapping of Riparian Zone Attributes Using Discrete Return Lidar, Quickbird and SPOT-5 Imagery: Assessing Accuracy and Costs." *Remote Sensing of Environment* 114 (11): 2679–2691. doi:10.1016/j.rse.2010.06.004.

Kane, V. R., J. A. Lutz, S. L. Roberts, D. F. Smith, R. J. McGaughey, N. A. Povak, and M. L. Brooks. 2013. "Landscape-Scale Effects of Fire Severity on Mixed-Conifer and Red Fir Forest Structure in Yosemite National Park." *Forest Ecology and Management* 287 (1): 17–31. doi:10.1016/j.foreco.2012.08.044.

Kane, V. R., M. P. North, J. A. Lutz, D. J. Churchill, S. L. Roberts, D. F. Smith, R. J. McGaughey, J. T. Kane, and M. L. Brooks. 2014. "Assessing Fire Effects on Forest Spatial Structure Using a Fusion of Landsat and Airborne Lidar Data in Yosemite National Park." *Remote Sensing of Environment* 151 (8): 89–101. doi:10.1016/j.rse.2013.07.041.

Kennedy, R. E., W. B. Cohen, and T. A. Schroeder. 2007. "Trajectory-Based Change Detection for Automated Characterization of Forest Disturbance Dynamics." *Remote Sensing of Environment* 110 (3): 370–386. doi:10.1016/j.rse.2007.03.010.

Korhonen, L., K. T. Korhonen, M. Rautiainen, and P. Stenberg. 2006. "Estimation of Forest Canopy Cover: A Comparison of Field Measurement Techniques." *Silva Fennica* 40 (4): 577. doi:10.14214/sf.315.

Korhonen, L., I. Korpela, J. Heiskanen, and M. Maltamo. 2011. "Airborne Discrete-Return LIDAR Data in the Estimation of Vertical Canopy Cover, Angular Canopy Closure and Leaf Area Index." *Remote Sensing of Environment* 115 (4): 1065–1080. doi:10.1016/j.rse.2010.12.011.

Kramer, H. A., B. M. Collins, M. Kelly, and S. L. Stephens. 2014. "Quantifying Ladder Fuels: A New Approach Using LiDAR." *Forests* 5 (6): 1432–1453. doi:10.3390/f5061432.

Li, P., and H. Xu. 2010. "Land-Cover Change Detection Using One-Class Support Vector Machine." *Photogrammetric Engineering & Remote Sensing* 76 (3): 255–263. doi:10.14358/PERS.76.3.255.

Li, X., and A. G. O. Yeh. 1998. "Principal Component Analysis of Stacked Multi-Temporal Images for the Monitoring of Rapid Urban Expansion in the Pearl River Delta." *International Journal of Remote Sensing* 19 (8): 1501–1518. doi:10.1080/014311698215315.

Liu, D., M. Kelly, and P. Gong. 2006. "A Spatial–Temporal Approach to Monitoring Forest Disease Spread Using Multi-Temporal High Spatial Resolution Imagery." *Remote Sensing of Environment* 101 (2): 167–180. doi:10.1016/j.rse.2005.12.012.

Lloyd, C. D., and P. M. Atkinson. 2002. "Deriving Dsms from Lidar Data with Kriging." *International Journal of Remote Sensing* 23 (12): 2519–2524. doi:10.1080/01431160110097998.

Lu, D., P. Mausel, E. Brondizio, and E. Moran. 2004. "Change Detection Techniques." *International Journal of Remote Sensing* 25 (12): 2365–2401. doi:10.1080/0143116031000139863.

Lucas, R. M., N. Cronin, A. Lee, M. Moghaddam, C. Witte, and P. Tickle. 2006. "Empirical Relationships between AIRSAR Backscatter and Lidar-Derived Forest Biomass, Queensland, Australia." *Remote Sensing of Environment* 100 (3): 407–425. doi:10.1016/j.rse.2005.10.019.

Lunetta, R. S., J. F. Knight, J. Ediriwickrema, J. G. Lyon, and L. D. Worthy. 2006. "Land-Cover Change Detection Using Multi-Temporal MODIS NDVI Data." *Remote Sensing of Environment* 105 (2): 142–154. doi:10.1016/j.rse.2006.06.018.

Mas, J.-F. 1999. "Monitoring Land-Cover Changes: A Comparison of Change Detection Techniques." *International Journal of Remote Sensing* 20 (1): 139–152. doi:10.1080/014311699213659.

Morsdorf, F., B. Kotz, E. Meier, K. I. Itten, and B. Allgower. 2006. "Estimation of LAI and Fractional Cover from Small Footprint Airborne Laser Scanning Data Based on Gap Fraction." *Remote Sensing of Environment* 104 (1): 50–61. doi:10.1016/j.rse.2006.04.019.

Nielsen, A. A. 2007. "The Regularized Iteratively Reweighted MAD Method for Change Detection in Multi-And Hyperspectral Data." *IEEE Transactions on Image Processing* 16 (2): 463–478. doi:10.1109/TIP.2006.888195.

Patra, S., S. Ghosh, and A. Ghosh. 2011. "Histogram Thresholding for Unsupervised Change Detection of Remote Sensing Images." *International Journal of Remote Sensing* 32 (21): 6071–6089. doi:10.1080/01431161.2010.507793.

Pettorelli, N., J. O. Vik, A. Mysterud, J.-M. Gaillard, C. J. Tucker, and N. C. Stenseth. 2005. "Using the Satellite-Derived NDVI to Assess Ecological Responses to Environmental Change." *Trends in Ecology & Evolution* 20 (9): 503–510. doi:10.1016/j.tree.2005.05.011.

Popescu, S. C., K. Zhao, A. Neuenschwander, and C. Lin. 2011. "Satellite Lidar Vs. Small Footprint Airborne Lidar: Comparing the Accuracy of Aboveground Biomass Estimates and Forest Structure Metrics at Footprint Level." *Remote Sensing of Environment* 115 (11): 2786–2797. doi:10.1016/j.rse.2011.01.026.

Prakash, A., and R. P. Gupta. 1998. "Land-Use Mapping and Change Detection in a Coal Mining Area - a Case Study in the Jharia Coalfield, India." *International Journal of Remote Sensing* 19 (3): 391–410. doi:10.1080/014311698216053.

Qin, Y., Z. Niu, F. Chen, B. Li, and Y. Ban. 2013. "Object-Based Land Cover Change Detection for Cross-Sensor Images." *International Journal of Remote Sensing* 34 (19): 6723–6737. doi:10.1080/01431161.2013.805282.

Remmel, T. K., and A. H. Perera. 2001. "Fire Mapping in a Northern Boreal Forest: Assessing AVHRR/NDVI Methods of Change Detection." *Forest Ecology and Management* 152 (1–3): 119–129. doi:10.1016/S0378-1127(00)00594-6.

Riano, D., F. Valladares, S. Condes, and E. Chuvieco. 2004. "Estimation of Leaf Area Index and Covered Ground from Airborne Laser Scanner (Lidar) in Two Contrasting Forests." *Agricultural and Forest Meteorology* 124 (3–4): 269–275. doi:10.1016/j.agrformet.2004.02.005.

Richardson, J. J., L. M. Moskal, and S. H. Kim. 2009. "Modeling Approaches to Estimate Effective Leaf Area Index from Aerial Discrete-Return Lidar." *Agricultural and Forest Meteorology* 149 (6–7): 1152–1160. doi:10.1016/j.agrformet.2009.02.007.

Ridd, M. K., and J. J. Liu. 1998. "A Comparison of Four Algorithms for Change Detection in an Urban Environment." *Remote Sensing of Environment* 63 (2): 95–100. doi:10.1016/S0034-4257(97)00112-0.

Schroeder, T. A., M. A. Wulder, S. P. Healey, and G. G. Moisen. 2011. "Mapping Wildfire and Clearcut Harvest Disturbances in Boreal Forests with Landsat Time Series Data." *Remote Sensing of Environment* 115 (6): 1421–1433. doi:10.1016/j.rse.2011.01.022.

Seto, K. C., C. E. Woodcock, C. Song, X. Huang, J. Lu, and R. K. Kaufmann. 2002. "Monitoring Land-Use Change in the Pearl River Delta Using Landsat TM." *International Journal of Remote Sensing* 23 (10): 1985–2004. doi:10.1080/01431160110075532.

Singh, A. 1989. "Review Article Digital Change Detection Techniques Using Remotely-Sensed Data." *International Journal of Remote Sensing* 10 (6): 989–1003. doi:10.1080/01431168908903939.

Sohl, T. L. 1999. "Change Analysis in the United Arab Emirates: An Investigation of Techniques." *Photogrammetric Engineering and Remote Sensing* 65 (4): 475–484.

Stephens, S. L., C. I. Millar, and B. M. Collins. 2010. "Operational Approaches to Managing Forests of the Future in Mediterranean Regions within a Context of Changing Climates." *Environmental Research Letters* 5 (2): 024003. doi:10.1088/1748-9326/5/2/024003.

Stephens, S. L., J. J. Moghaddas, C. Edminster, C. E. Fiedler, S. Haase, M. Harrington, J. E. Keeley, et al. 2009. "Fire Treatment Effects on Vegetation Structure, Fuels, and Potential Fire Severity in Western US Forests." *Ecological Applications* 19 (2): 305–320. doi:10.1890/07-1755.1.

Su, Y., Q. Guo, D. L. Fry, B. M. Collins, M. Kelly, J. P. Flanagan, and J. J. Battles. 2016. "A Vegetation Mapping Strategy for Conifer Forests by Combining Airborne LiDAR Data and Aerial Imagery." *Canadian Journal of Remote Sensing* 42 (1): 1–15. doi:10.1080/07038992.2016.1131114.

Tilley, B. K., I. A. Munn, D. L. Evans, R. C. Parker, and S. D. Roberts. 2004. "Cost Considerations of Using Lidar for Timber Inventory." Paper presented at the Southern Forest Economics Workshop, St. Augustine, FL, March 14–16.

Walter, V. 2004. "Object-Based Classification of Remote Sensing Data for Change Detection." *ISPRS Journal of Photogrammetry and Remote Sensing* 58 (3–4): 225–238. doi:10.1016/j.isprsjprs.2003.09.007.

Weishampel, J. F., J. B. Blair, R. Knox, R. Dubayah, and D. Clark. 2000. "Volumetric Lidar Return Patterns from an Old-Growth Tropical Rainforest Canopy." *International Journal of Remote Sensing* 21 (2): 409–415. doi:10.1080/014311600210939.

Yousif, O., and Y. F. Ban. 2013. "Improving Urban Change Detection from Multitemporal SAR Images Using PCA-NLM." *IEEE Transactions on Geoscience and Remote Sensing* 51 (4): 2032–2041. doi:10.1109/TGRS.2013.2245900.

Yu, X., J. Hyyppä, H. Kaartinen, and M. Maltamo. 2004. "Automatic Detection of Harvested Trees and Determination of Forest Growth Using Airborne Laser Scanning." *Remote Sensing of Environment* 90 (4): 451–462. doi:10.1016/j.rse.2004.02.001.

Yu, X., J. Hyyppa, A. Kukko, M. Maltamo, and H. Kaartinen. 2006. "Change Detection Techniques for Canopy Height Growth Measurements Using Airborne Laser Scanner Data." *Photogrammetric Engineering and Remote Sensing* 72 (12): 1339–1348. doi:10.14358/PERS.72.12.1339.

Zhang, X., P. Xiao, and X. Feng. 2013. "Impervious Surface Extraction from High-Resolution Satellite Image Using Pixel-And Object-Based Hybrid Analysis." *International Journal of Remote Sensing* 34 (12): 4449–4465. doi:10.1080/01431161.2013.779044.

Zhao, K., and S. Popescu. 2009. "Lidar-Based Mapping of Leaf Area Index and Its Use for Validating GLOBCARBON Satellite LAI Product in a Temperate Forest of the Southern USA." *Remote Sensing of Environment* 113 (8): 1628–1645. doi:10.1016/j.rse.2009.03.006.

Zhao, K., S. Popescu, and R. Nelson. 2009. "Lidar Remote Sensing of Forest Biomass: A Scale-Invariant Estimation Approach Using Airborne Lasers." *Remote Sensing of Environment* 113 (1): 182–196. doi:10.1016/j.rse.2008.09.009.

Zimble, D. A., D. L. Evans, G. C. Carlson, R. C. Parker, S. C. Grado, and P. D. Gerard. 2003. "Characterizing Vertical Forest Structure Using Small-Footprint Airborne Lidar." *Remote Sensing of Environment* 87 (2–3): 171–182. doi:10.1016/S0034-4257(03)00139-1.